OPEN ACCESS
IOP Publishing
Journal of Physics D: Applied Physics
J. Phys. D: Appl. Phys. **57** (2024) 455201 (18pp)
https://doi.org/10.1088/1361-6463/ad6881

Effects of spatiotemporal plasma power distribution on the modeling of ignition kernel evolution in quiescent and turbulent methane/air mixtures

Praise Noah Johnson, Taaresh Sanjeev Taneja and Suo Yang*

Department of Mechanical Engineering, University of Minnesota—Twin Cities, Minneapolis, MN 55455, United States of America

E-mail: suo-yang@umn.edu

Received 1 May 2024, revised 11 July 2024
Accepted for publication 29 July 2024
Published 14 August 2024

Abstract

The present work improves a phenomenological plasma-assisted combustion model by integrating the spatiotemporal distribution of plasma power density, thereby considering the evolution of plasma streamers in the modeling, and subsequently, better predicting the ignition kernel evolution. The improved phenomenological model is validated against experiments representing the plasma discharge and post-discharge ignition kernel evolution. Specifically, the new model demonstrates a more accurate prediction of ultrafast gas heating and O_2 dissociation during the plasma discharge, compared to the original model. In addition, the new model is found to closely match the experimental pressure wave and heated channel profiles post-discharge without the need for tuning the energy deposition (unlike the original model), highlighting its accuracy of post-discharge ignition kernel dynamics. The improved phenomenological model is then employed to investigate ignition kernel evolution for a stoichiometric methane-air discharge across various discharge gap configurations. Simulations reveal a non-uniform temperature and streamer distribution progressing from the electrode tips toward the center, contrasting uniform cylindrical discharges previously described in the original model. Streamer propagation is observed to be faster for larger gaps when maintained at the same average electric field for different discharge gaps. The tendency of smaller gaps to produce detached toroidal ignition kernels is observed, while larger gaps promote cylindrical and attached ignition kernels. Interactions between successive ignition kernels from consecutive discharges varied significantly, with the smallest gap (1 mm) promoting the quenching of the preceding ignition kernel due to the initial kernel–kernel separation. The intermediate gap (2 mm) promotes detached kernel growth. In contrast, in the largest gap (4 mm), kernels consistently combine and expand attached to electrodes. The impact of homogeneous isotropic turbulence is also explored, showing the persistence of ignition kernels early on but eventually quenching due to enhanced radical and heat losses with pronounced turbulence intensity.

* Author to whom any correspondence should be addressed.

Keywords: plasma-assisted ignition, methane ignition, plasma power density, nanosecond pulsed discharges, ignition kernel evolution, homogeneous isotropic turbulence (HIT)

1. Introduction

Low-temperature plasmas provide an inimitable possibility of improving combustion characteristics, such as ignition, flame stability, and emission control [1–5], particularly in low-temperature combustion systems, thereby aiding the adherence of combustion systems to ever-stringent emission and performance standards [6, 7]. In particular, nanosecond repetitively pulsed (NRP) plasma discharges in low-temperature fuel-air mixtures result in the production of reactive radicals, charged and excited species, in addition to the fast and slow heating of the gas mixture due to the relaxation of electronically and vibrationally excited states, respectively [5, 8, 9]. The production of reactive radicals and simultaneous gas heating enhance the mixture's reactivity, affecting ignition, flame stability, and emissions in plasma-assisted combustion (PAC) systems [10–15]. Thus, it is imperative to numerically investigate PAC systems and their effects on the physical and chemical properties of the gas mixture for practical applications.

Despite the necessity to explore the science involved in PAC processes, modeling a PAC system presents a monumental challenge with the innate intricacies of various physical and chemical phenomena. This involves the complex intercoupling of gas-phase and plasma-phase chemistry, electrodynamics, and transport processes, spanning diverse length and time scales [16]. The reaction types specific to plasma chemistry involve electron impact excitations, ionization, and dissociations, followed by de-excitation/relaxation, attachment, and dissociation reactions [17]. The inclusion of the various electron impact reactions, whose rates depend on the reduced electric field (E/N) and cross sections of the colliding species, and the subsequent follow-up reactions brings additional complexity to modeling plasma, in addition to modeling the conventional gas-phase chemistry and flow conservation equations. The simplest models involve 0D calculations of plasma where the transport of plasma is not considered [18–20]; instead, only the plasma chemistry is accounted for using a Boltzmann-based solver like BOLSIG [21]. While these models provide valuable information regarding chemistry aspects such as ignition, NOx formation in carbon-free ammonia, and fuel reforming improvements [19, 22, 23], they cannot predict the complex spatiotemporal behavior of plasma. To account for these complexities, several studies [16, 24–27] investigated the computational modeling of plasma at varying levels of details. The modeling of low-temperature plasma can be classified into three distinct categories, namely: (i) kinetic/particle models [25]; (ii) fluid models [26, 27]; and (iii) phenomenological models [24, 28, 29] with decreasing order of details and computational cost. Kinetic models involve a Lagrangian formulation of particles and are successful in resolving kinetic behavior and multi-scale dynamics in plasma [25, 30, 31], by providing a detailed resolution of individual particle dynamics thereby demanding significant computational resources. In contrast, the fluid model treats the plasma as a continuum based on the macroscopic behavior [26, 27, 32–34], offering a simpler mathematical framework suitable for large-scale simulations. Both the kinetic and fluid models capture the overall behavior and evolution of plasma discharges over time. Despite their fidelity, kinetic and fluid models present a formidable assignment in simulating practical configurations of NRP discharges in PAC applications. Consequently, phenomenological models [24, 28, 29, 35], which are computationally least expensive compared to kinetic and fluid models, yet able to capture the fundamental processes of species dissociation and gas heating imparted by NRP plasma discharges, were developed making the simulation of practical PAC systems feasible.

In particular, Castela *et al* [24] proposed a phenomenological PAC model that captures the primary effects involved in NRP discharges, by quantifying the discharge energy fraction for each effect. These effects involved two gas heating mechanisms: (i) the ultrafast gas heating from the relaxation of electronically excited N_2 ($N_2(e) + O_2 \rightarrow N_2 + 2O$+heat);(ii)the ultrafast vibrational energy excitation of N_2 ($e^- + N_2 \rightarrow N_2(v) + e^-$), followed by the slow gas heating from the vibrational-to-translational (V-T) relaxation [36, 37] ($N_2(v) + X \rightarrow N_2 + X +$ heat). In addition, the chemical effects of plasma were considered in the model by accounting for the ultrafast dissociation of O_2 to O radicals driven by the electronic excited states of N_2 ($N_2(e) + O_2 \rightarrow N_2 + 2\,O +$ heat). The simplifications of plasma processes in the phenomenological model therefore enabled direct numerical simulations (DNS) of plasma-assisted ignition in turbulent reacting flows [24, 28, 38]. Supplementing the studies by Castela *et al* [24, 38], several studies [39–43] involving the large eddy simulations of PAC ignition followed up utilizing the aforementioned approach to model plasma discharges. In addition to utilizing the phenomenological model for plasma-assisted ignition investigations, a recent study conducted by the authors extended its application to reforming mixtures, enabling the investigation of CH_4 reforming in the complete absence of O_2 [35]. Despite the surge in interest in the phenomenological model [24], the model was limited to the primary assumption that chemical effects in O_2 chemistry would be dominant for fresh gas mixtures. Moreover, the model does not consider the effects of E/N and its spatiotemporal distribution on discharge energy fractions.

In a recent study, Barléon *et al* [29] proposed an extended phenomenological model named PACMIND (PAC phenoMenological modelIng for non-equilibrium discharges) to account for all the dominant kinetic effects along with fast and slow gas heating. Besides, the effect of E/N on discharge energy fractions was accounted for by considering a look-up approach for the energy fractions for various E/N values across the reactive kernel, a significant improvement over the original model [24]. Regardless of these appreciable improvements over the model proposed by Castela *et al* [24], the study utilized a time-averaged spatial distribution of plasma power density (PPD), which was assumed to be the same for all plasma time steps. Such assumptions regarding the time-averaged spatial distribution of PPD may be sufficiently robust for gaining a qualitative understanding of post-discharge ignition kernel dynamics. Following the development of PACMIND [29], subsequent research [44, 45] further ulilized this improved model to investigate flame stabilization in a swirl burner and NOx formation in a sequential combustor using NRP discharges. Often, atmospheric or higher-pressure plasmas involve the development and propagation of fast-moving ionization fronts called 'streamers', that are transient and filamentary [46–48]. Such streamers institute high electric fields and electron energies locally and are precursors to spark formation—a channel of large electric current flow and heat release. The formation and evolution of streamers and the subsequent spark formation enable the chemical breakdown of surrounding molecules, invigorating the local chemical reactivity [49]. It is therefore important to numerically investigate the spatiotemporal dynamics of plasma streamers and the subsequent spark formation in combustible gas mixtures to understand the effect of streamers on the chemistry and flow behavior and vice versa. However, capturing the streamer evolution during the pulse requires accounting for the accurate development of electron densities and electric fields in time, which are also found to differ significantly at different input voltages [50, 51]. Consequently, resolving the spatiotemporal dynamics of plasma streamers requires an efficient numerical treatment to solve Poisson's equation and account for photoionization effects [52]. Despite the plethora of studies investigating the implementation of Poisson's equation and photoionization effects [52–55], phenomenological models cannot afford these implementations owing to the computational complexity inherent in these models. As the streamer evolution and the streamer-to-spark transition depend on precisely incorporating time-varying plasma characteristics during the pulse discharge (hereafter mentioned as either pulse-phase or discharge-phase) [56–58], it is essential to accommodate the time-varying plasma behavior in the phenomenological model to accurately model the streamer evolution and its impact on the ignition kernel and flame evolution.

The present study aims to incorporate the time-varying PPD from detailed fluid simulations into the phenomenological model of Castela *et al* [24] to capture the spatiotemporal evolution of streamers and ignition kernels. Subsequently, the plasma-assisted ignition of methane/air mixtures will be numerically investigated using the DNS of the improved phenomenological model, for different gap distances in quiescent and turbulent methane/air mixtures. The present work is among the foremost to investigate the spatiotemporal evolution of streamers to improve the original phenomenological model [24] to simulate PAC. The methodology discussed herein represents an effort to enhance the physical accuracy of phenomenological plasma models and complements recent advancements [29, 44, 45] in the literature aimed at improving the original phenomenological model [24].

The remainder of this article is organized as follows: section 2 briefly discusses the numerical framework of the phenomenological model, along with the incorporation of spatiotemporal variation of PPD in the present work. Following, the validation of the improved phenomenological model against experiments is presented in section 3.1. The numerical results of ignition kernel development in quiescent and turbulent methane/air mixtures are presented in the remainder of section 3, following which, the conclusions are summarized in section 4.

2. Model description and methodology

The phenomenological NRP plasma model proposed by Castela *et al* [24] has been adapted in the present work to model the plasma-assisted ignition of methane/air mixtures. The model discussed herein has been implemented in-house [28, 41] on the OpenFOAM [59] platform. The present study did not consider electrode heating due to the short discharge duration of a few nanoseconds and the rapid movement of the highest temperature zones away from the electrodes within 100 μs, which is much smaller than the conduction timescale of about a millisecond at the electrode tip. A full description of the original model can be found in Castela *et al* [24, 38]. Nevertheless, a brief description of the original phenomenological model (section 2.1) is included below for self-containment, along with the improved PPD distribution (section 2.2) of the present work.

2.1. Phenomenological NRP model

When the NRP discharges in air and fuel-air mixtures are characterized by a reduced electric field (E/N) ranging from 100 to 400 Td (1 Td $= 10^{-17}$V cm^2), about 90% of the deposited pulse energy $\dot{E}_\mathrm{p}$ is found to be stored in the vibrational and electronic modes of N_2 [24]. The vibrational excitation of N_2 in a stoichiometric CH_4/air mixture occurs in a few 10's of nanoseconds, and the corresponding vibrational-to-translational (V-T) de-excitation occurs in much longer microsecond time scales. These two-step phenomena of slow gas heating are depicted by: $N_2 + e^- \rightarrow N_2(v) + e^-$ (ultrafast increase in vibrational energy), followed by $N_2(v) + X \rightarrow N_2 + X +$ Heat (slow heating due to V-T relaxation). Here, $N_2(v)$ represents a general vibrational state of N_2 and X being any species. Unlike V-T relaxation, the electronic excitation

of N_2 to $N_2(e)$ and subsequent dissociation of O_2 to two O radicals during the relaxation of $N_2(e)$ occurs in a few 10's nanoseconds, thereby resulting in ultrafast dissociation of O_2 and ultrafast gas heating, as shown by the following consecutive reactions: $N_2 + e^- \rightarrow N_2(e) + e^-$ and $N_2(e) + O_2 \rightarrow N_2 + 2\,O + \text{Heat}$. The remaining discharge energy (∼10%) contributes to processes such as ionization, excitation of O_2 and CH_4, and dissociation of CH_4. These comparatively smaller fractions were neglected in both the original [24] and present phenomenological model for simplicity.

Thus, the deposited plasma energy $\dot{E}_\mathrm{p}$ is divided into three components, contributing to ultrafast gas heating ($\dot{E}_\mathrm{p,heat}$), ultrafast O_2 dissociation ($\dot{E}_\mathrm{p,diss}$), and ultrafast increase in the vibrational energy of N_2 ($\dot{E}_\mathrm{p,vib}$) as given by equation (1):

$$\dot{E}_\mathrm{p} = \dot{E}_\mathrm{p,heat} + \dot{E}_\mathrm{p,diss} + \dot{E}_\mathrm{p,vib}. \tag{1}$$

The set of governing equations solved by accounting for the three major effects of NRP discharges are given below:

$$\frac{\partial \rho}{\partial t} + \frac{\partial (\rho u_i)}{\partial x_i} = 0 \tag{2}$$

$$\frac{\partial (\rho u_j)}{\partial t} + \frac{\partial (\rho u_i u_j)}{\partial x_i} = -\frac{\partial p}{\partial x_j} + \frac{\partial \tau_{ij}}{\partial x_i} \tag{3}$$

$$\frac{\partial (\rho Y_k)}{\partial t} + \frac{\partial (\rho u_i Y_k)}{\partial x_i} = -\frac{\partial}{\partial x_j}(\rho V_{k,i} Y_k) + W_k \dot{\omega}_k^c + W_k \dot{\omega}_k^p \tag{4}$$

$$\frac{\partial (\rho h)}{\partial t} + \frac{\partial (\rho u_i h)}{\partial x_i} = -\frac{\partial q_i}{\partial x_j} + \frac{\partial (\tau_{ij} u_i)}{\partial x_i} + \frac{\partial p}{\partial t} - \frac{\partial}{\partial x_i} \times \left(\rho \sum_{k=1}^{N_\mathrm{sp}} h_{s,k} Y_k V_{k,i} \right) + \dot{Q}_\mathrm{react} + \dot{E}_\mathrm{p,heat} + \dot{R}^p_\mathrm{VT}. \tag{5}$$

Equations (2)–(5) represent the continuity, momentum, species, and energy conservation equations with appropriate additional source terms to accommodate the effects of NRP discharges. In the above equations, ρ and p denote the density and pressure, while u_i and q_i represent the velocity and heat flux vector in the ith direction. τ_{ij} represents the viscous stress tensor, whereas Y_k, W_k, and $V_{k,i}$ represents the mass fraction, molar mass, and diffusion velocity in the ith direction respectively, for the kth species. In equation (4), $\dot{\omega}_k^p$ denotes the molar production rate to model the production of species by ultrafast dissociation of gas species (O_2 dissociation in the present work), while $\dot{\omega}_k^c$ denotes the molar production rate due to gas-phase reactions. In equation (5), h denotes the total/stagnation non-chemical enthalpy per unit mass and is given by $h_s + \frac{1}{2} u_i u_i$, where h_s represent the sensible enthalpy per unit mass. The slow gas heating due to V-T relaxation of $N_2(v)$ is accounted for by adding a vibrational energy relaxation rate $\dot{R}^p_\mathrm{VT}$ to the energy equation (see equation (5)). In order to track the vibrational energy $\dot{E}_\mathrm{p,vib}$ and the corresponding V-T relaxation rate $\dot{R}^p_\mathrm{VT}$, an additional conservation equation (see equation (6)) for the specific vibrational energy e_vib carried by N_2 molecules is added to the system:

$$\frac{\partial (\rho e_\mathrm{vib})}{\partial t} + \frac{\partial (\rho u_i e_\mathrm{vib})}{\partial x_i} = -\frac{\partial}{\partial x_j}\left(\rho D_{N_2} \frac{\partial e_\mathrm{vib}}{\partial x_i} \right) + \dot{E}_\mathrm{p,vib} - \dot{R}^p_\mathrm{VT} \tag{6}$$

To close this model, we assume a fraction α of $\dot{E}_\mathrm{p}$ contributing to the electronic excitation of N_2, thereby resulting in ultrafast dissociation ($\dot{E}_\mathrm{p,diss}$) and ultrafast heating ($\dot{E}_\mathrm{p,heat}$) as given by

$$\dot{E}_\mathrm{p,heat} + \dot{E}_\mathrm{p,diss} = \alpha \dot{E}_\mathrm{p}. \tag{7}$$

In addition, $\dot{E}_\mathrm{p,heat}$ and $\dot{E}_\mathrm{p,diss}$ can be expressed as:

$$\dot{E}_\mathrm{p,heat} = g_\mathrm{heat} \dot{E}_\mathrm{p}; \tag{8}$$

$$\dot{E}_\mathrm{p,diss} = g_\mathrm{diss} \dot{E}_\mathrm{p}, \tag{9}$$

where g_heat and g_diss denotes the fraction of $\dot{E}_\mathrm{p}$ used for ultrafast heating and dissociation, respectively. Using equations (8) and (9), $\dot{E}_\mathrm{p,vib}$ can be expressed as:

$$\dot{E}_\mathrm{p,vib} = [1 - (g_\mathrm{heat} + g_\mathrm{diss})]\, \dot{E}_\mathrm{p}. \tag{10}$$

If $h_{f,k}$ is the specific formation enthalpy of species k, then $\dot{E}_\mathrm{p,diss}$ can also be given by

$$\dot{E}_\mathrm{p,diss} = \sum_{k=1}^{N_\mathrm{sp}} h_{f,k} \dot{\omega}_k^p = \sum_{k=1}^{N_\mathrm{sp}} g_\mathrm{diss}^k \dot{E}_\mathrm{p}, \tag{11}$$

where g_diss^k denotes the fraction of $\dot{E}_\mathrm{p}$ expend to produce species k. Therefore, the species production rate by plasma $\dot{\omega}_k^p$ for a species k is given by equation (12):

$$\dot{\omega}_k^p = g_\mathrm{diss}^k \frac{\dot{E}_\mathrm{p}}{h_{f,k}}. \tag{12}$$

g_diss^k is assumed to be proportional to $Y_{O_2}/Y^f_{O_2}$, where $Y^f_{O_2}$ is the mass fraction of O_2 in the fresh mixture. The proportionality constant $Y_{O_2}/Y^f_{O_2}$ is utilized to ensure that $\dot{E}_\mathrm{p,diss}$ approaches zero as Y_{O_2} tends to zero (representing a burnt gas mixture), and reaches its maximum value when $Y_{O_2} = Y^f_{O_2}$ (indicating a fresh gas mixture). If η is the fraction of $\dot{E}_\mathrm{p}$ leading to O_2 dissociation in a fresh gas mixture, g_diss^k can then be written as given in equation (13):

$$g_\mathrm{diss}^k = \eta \frac{Y_{O_2}}{Y^f_{O_2}}. \tag{13}$$

Since we consider the dissociation of O_2 to two O radicals, the conservation of mass involving plasma reactions give

$$\dot{\omega}^p_{O_2} = -\frac{W_O}{W_{O_2}} \dot{\omega}^p_O. \tag{14}$$

Combining the mass conservation equation represented in equation (14) (for the process $O_2 \rightarrow O$) with equation (11), and subsequently substituting the expression for $\dot{\omega}_O^p$ derived from equations (12) and (13), we observe

$$\begin{aligned}\dot{E}_{\mathrm{p,diss}} &= h_{f,O}\dot{\omega}_O^p - h_{f,O_2}\frac{Y_{O_2}}{Y_{O_2}^f}\dot{\omega}_O^p \\ &= \eta\frac{Y_{O_2}}{Y_{O_2}^f}\left[1 - \frac{W_O}{W_{O_2}}\frac{h_{f,O_2}}{h_{f,O}}\right]\dot{E}_\mathrm{p}. \end{aligned} \tag{15}$$

Using the above expression for $\dot{E}_{\mathrm{p,diss}}$, $\dot{E}_{\mathrm{p,heat}}$ and $\dot{E}_{\mathrm{p,vib}}$ can be obtained as:

$$\dot{E}_{\mathrm{p,heat}} = \left\{\alpha - \eta\frac{Y_{O_2}}{Y_{O_2}^f}\left[1 - \frac{W_O}{W_{O_2}}\frac{h_{f,O_2}}{h_{f,O}}\right]\right\}\dot{E}_\mathrm{p}; \tag{16}$$

$$\dot{E}_{\mathrm{p,vib}} = (1-\alpha)\,\dot{E}_\mathrm{p}. \tag{17}$$

In equations (5) and (6), $\dot{R}_{\mathrm{VT}}^p$ is calculated using the Landau–Teller harmonic oscillator approach as given by

$$\dot{R}_{\mathrm{VT}}^p = \rho\frac{e_{\mathrm{vib}} - e_{\mathrm{vib}}^{\mathrm{eq}}(T)}{\tau_{\mathrm{VT}}}, \tag{18}$$

where $e_{\mathrm{vib}}^{\mathrm{eq}}(T)$ denotes the equilibrium vibrational energy of a mixture at a given temperature T and is given by:

$$e_{\mathrm{vib}}^{\mathrm{eq}}(T) = \frac{R\Theta_1}{e^{\frac{\Theta_1}{T}} - 1}, \tag{19}$$

where Θ_1 is the vibrational temperature corresponding to the first quantum vibrational state of N_2, and gas constant of the mixture $R = \frac{R_u}{W_{N_2}}$ (R_u being the universal gas constant). In equation (18), τ_{VT} is given by:

$$\tau_{\mathrm{VT}} = \left(\frac{1}{\tau_{\mathrm{VT}}^{\mathrm{O}}} + \frac{1}{\tau_{\mathrm{VT}}^{\mathrm{O_2}}} + \frac{1}{\tau_{\mathrm{VT}}^{N_2}}\right)^{-1}, \tag{20}$$

and

$$\tau_{\mathrm{VT}}^k = \frac{c}{p_k}e^{\left[a_k\left(T^{\frac{-1}{3}} - b_k\right) - 18.42\right]}. \tag{21}$$

In equations (20) and (21), τ_{VT}^k is the V-T relaxation time of N_2(v) by collision with species k, c = 1 atm-s, p_k is the partial pressure of species k, and a_k and b_k are the experimental constants as given in Millikan and White [60].

2.2. PPD distribution mapping

The phenomenological model proposed by Castela *et al* [24] considered a PPD $\dot{E}_\mathrm{p}$ distribution invariant in time. Spatially, the PPD was assumed to be distributed proportionally to a complementary error function *erfc*(). If σ_p is the discharge energy per unit volume ($\mathrm{J\,m^{-3}}$) and τ_p is the characteristic time of the plasma pulse, which is defined as the time duration for which the plasma discharge occurs, then the PPD distribution was obtained using

$$\dot{E}_\mathrm{p} = \frac{\sigma_p}{\tau_p}\mathrm{erfc}\left(\frac{r^2}{a}\right)^b, \tag{22}$$

where r represents the radial distance from the discharge axis, and a and b are constants chosen based on the geometric configuration. The behavior of the spatial distribution function is shown in figure 1(a) by plotting the PPD distribution in equation (22) normalized with σ_p/τ_p, and the distribution is observed to peak at the discharge center and plummets to zero radially. The PPD distribution obtained using this formulation in Castela *et al* [24] is shown in figure 1(b). Albeit the simplicity, the assumption of time invariance and the error function-based spatial distribution forsake the intrinsic non-linearities in plasma discharges, thereby introducing inaccuracies in predicting streamer dynamics (as will be discussed in section 3.2). Considering that the phenomenological framework models the plasma-specific source terms based on the PPD $\dot{E}_\mathrm{p}$ and since σ_p (and thereby, $\dot{E}_\mathrm{p}$) is the only plasma-specific user input in the model, any adaptation to encompass the plasma-specific non-linearities in the present form of the phenomenological model should begin with a more accurate implementation of the PPD distribution.

Figure 2 shows the evolution of PPD and the electron number density between an axisymmetric pip-pin electrode configuration for a discharge gap of 1 mm and an applied voltage of 5 kV. The computations are performed using a fluid/continuum-based non-thermal plasma code, PASSKEy [34], for a discharge in air. At 1 ns, contours of electron-dense fronts are observed to localize near the electrodes (see figure 2(a)). As time progresses (3 ns), these electron-dense fronts propagate to the opposite electrode, establishing a connection. As the time increases further (10 ns), the previously established channel witnesses an increase in electron number densities ($\sim 10^{22}\#/m^3$). This early propagation of electron-rich fronts, followed by the connection of opposing fronts, and the steady increase of electron flow over time within this channel depicts the streamer head propagation and spark formation (marked by the connection of opposing streamer head and subsequent amplification of current/temperature in the channel) during the nanosecond discharge (see figure 2(a)). Upon observing the PPD evolution portrayed in figure 2(b), similar dynamics can be observed at similar time scales, illustrating the streamer head propagation, connection, and spark formation. Thus to encapsulate the dynamics of streamer evolution in the phenomenological model, it is therefore sufficient to simply incorporate the spatiotemporal evolution of PPD in the phenomenological model.

In consideration of the above observation, the present study therefore utilizes the spatiotemporal variation of PPD obtained from fluid/continuum-based plasma modeling in the phenomenological model. Fluid/continuum-based 2D axisymmetric simulations of plasma discharge in the air are performed using PASSKEy [34] for the gap distance and applied voltage of interest. The utilization of a 2D axisymmetric assumption,

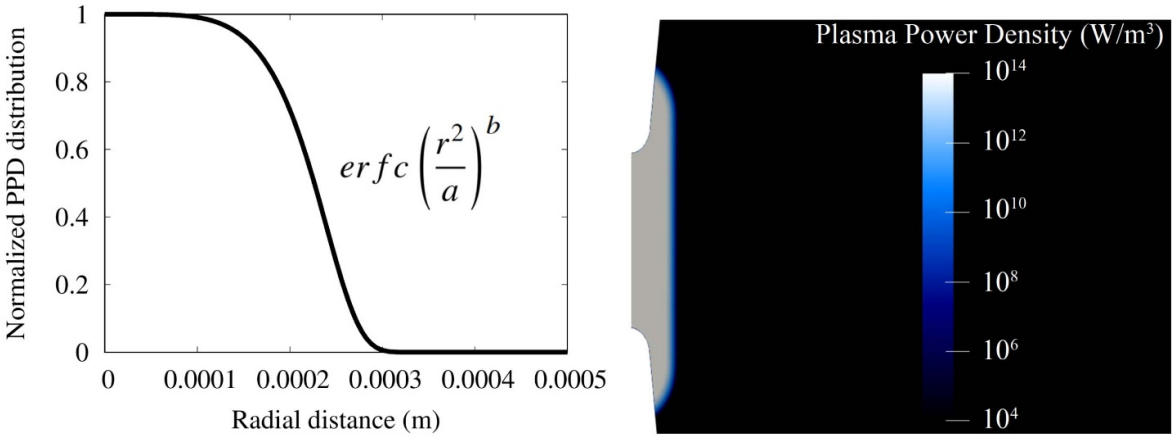

(a) Normalized radial distribution of PPD (b) PPD contour (W/m^3)

Figure 1. (a) Radial distribution of plasma power density (PPD) normalized with σ_p/τ_p; and (b) Plasma power density (PPD) ($\mathrm{W\,m^{-3}}$) contour in the original phenomenological model [24].

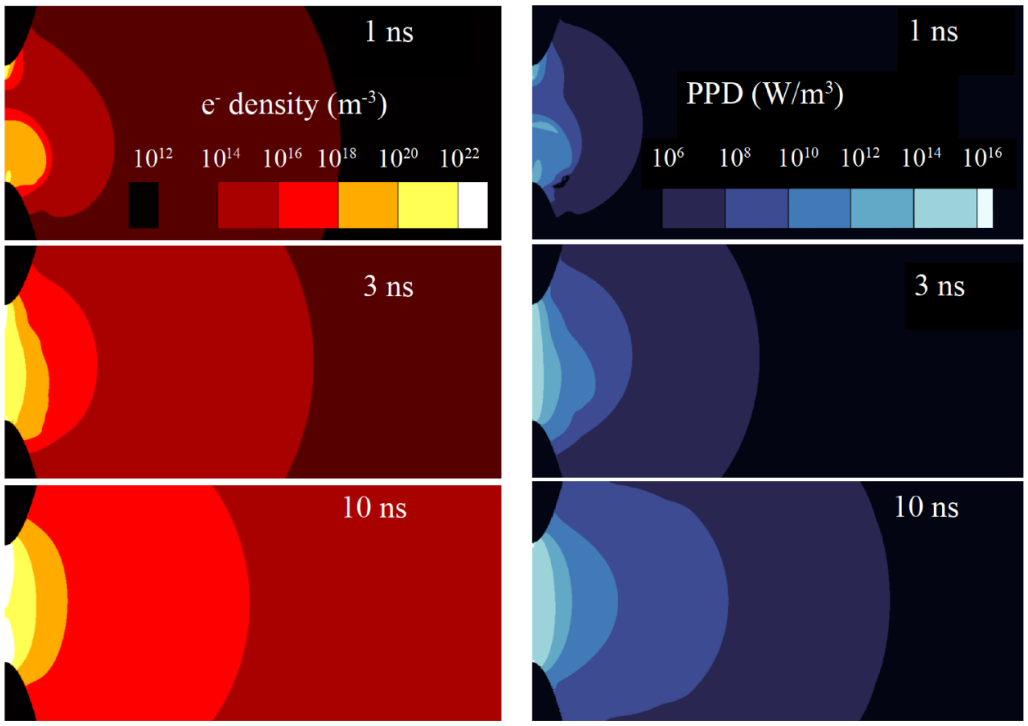

(a) Electron density (m^{-3}) (b) PPD (W/m^3)

Figure 2. The evolution of (a) electron number density ($\mathrm{m^{-3}}$) and (b) plasma power density (PPD, $\mathrm{W\,m^{-3}}$) obtained from 2D axisymmetric plasma fluid simulations using PASSKEy [34].

coupled with the choice of air as the simulation medium, is justified by the symmetrical nature of the system along the discharge axis and the similarity of air's constituent elements to those in fuel-air mixtures, respectively, enabling efficient and accurate modeling of plasma discharge. Thus, the two primary assumptions of the present model are (i) air plasma discharge behaving closely to that of the CH_4-air plasma discharge, given the relatively minor mass fraction of CH_4 ($\sim$0.055) compared to those of O_2 and N_2, and (ii) the axisymmetric assumption along the discharge axis, due to the axisymmetry of the configuration and the absence of a mean flow. Simulations are performed under local mean energy approximation and Poisson's equation is solved explicitly by enforcing dielectric relaxation time (calculated using ϵ/σ, where, ϵ is the permittivity of the medium and σ is the plasma conductivity). The photoionization effect is implemented using the classical three-exponential Helmholtz model [34, 61, 62]. All simulations to obtain the 2D PPD are performed at 300 K and 1 atm. The generated time-evolving 2D axisymmetric PPD distribution is then interpolated onto a cylindrical mesh to construct

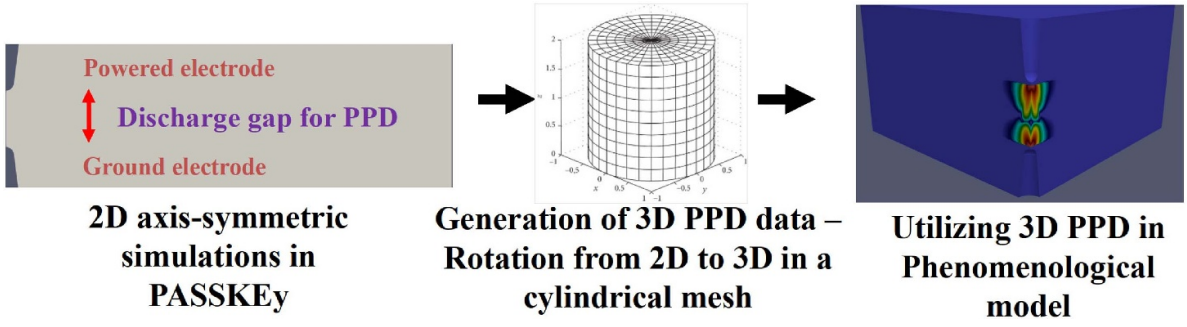

Figure 3. A schematic depicting the generation of a time series of 3D plasma power density (PPD) distribution for the utilization in the present phenomenological model from detailed 2D axisymmetric air discharge simulations.

a 3D distribution of PPD in space, which is also temporally evolving. This spatiotemporal distribution in a cylindrical mesh is subsequently mapped onto the 3D geometry of interest in the phenomenological model. This procedure of obtaining a time series of 3D PPD to be utilized in the phenomenological model is depicted in figure 3.

2.3. Numerical setup

Three distinct computational geometries with discharge gaps of 1 mm, 2 mm, and 4 mm are considered in the present work to investigate NRP plasma discharges in stoichiometric methane/air mixture at 300 K and atmospheric pressure. The investigations in the present work are done on an octant sector of the respective pin-to-pin geometry. The mesh contains 3.1, 4, and 5.8 million hexahedral cells for 1 mm, 2 mm, and 4 mm discharge gaps, respectively, with the smallest cell size of 7 μm (along the radial direction) near the discharge center, and a maximum cell size of 35 μm near the boundaries in the radial direction. Along the axial direction, the cell size varies between 7 μm near the electrodes to 35 μm at the boundary. The outflow boundaries of the cylinder are maintained using wave transmissive boundary conditions (non-reflecting boundary condition) [64] to permit the propagation of the ignition kernel without being reflected back. The electrodes are considered with no-slip velocity boundary conditions along with zero-gradient boundary conditions for all other fields, All other faces are maintained as symmetric boundaries. Second-order, total variation diminishing, central difference schemes were used for the gradient, divergence, and Laplacian terms of all the governing equations. The gas-phase chemistry model used for methane/air mixture is a reduced version [65] of the GRI 3.0 mechanism [66] containing 30 species and 325 reactions. The thermodynamic properties of the species included were only available up to 5000 K (T_{high}). Beyond T_{high}, the present work linearly extrapolates the thermodynamic properties from the corresponding value at T_{high} using the expression $X(T) = X(T_{\text{high}}) + \left(\frac{\mathrm{d}X}{\mathrm{d}T}\right)_{T_{\text{high}}} \times (T - T_{\text{high}})$ when $T > T_{\text{high}}$. In the above equation, X is the thermodynamic property of interest (such as c_p, h, etc). This linear extrapolation is based on the observed linear-to-logarithmic behavior of the thermodynamic properties in the range of 3000 – 10 000 K [67–70]. Consequently, beyond 5000 K, the thermodynamic properties are not accurate and can only be considered as a first-order approximation from 5000 K to the desired temperature. For the NRP discharges, the pulse width is fixed to 20 ns, 11 ns, and 7 ns, respectively, and the applied voltage is 5 kV, 10 kV, and 20 kV, respectively, for 1 mm, 2 mm, and 4 mm discharge gaps. The pulse width and applied voltage for three geometries was decided accordingly to limit the energy deposited per pulse to 1.5 mJ, 3 mJ, and 6 mJ, respectively (energies being scaled linearly with the discharge volume) at an average reduced electric field (E/N) of $\sim$200 Td (1 Td $= 10^{-17}$ V cm^2). The time step during the plasma discharge is fixed at 0.5 ns and is allowed to vary in the gap based on the CFL number (CFL $\leqslant 0.5$).

3. Results and discussion

3.1. Model validation against experiments

The phenomenological model adapted for the spatiotemporal variation of PPD can now be validated for its fidelity against experiments available in the literature. The validation study is performed for two distinct phases in an NRP discharge—the discharge phase (nanosecond timescales during discharge) and the gap phase (microsecond timescales post-discharge) to gauge the accuracy of the present model during and post-discharge.

Firstly, the temporal evolution of gas temperature and O radical concentration in an air plasma discharge [36] is used to validate the accuracy of the present model during the discharge phase. Figure 4 presents the evolution of temperature and O radical concentration obtained using the improved phenomenological model (solid red lines) compared against the original phenomenological model (dashed black lines) [24] and the experiments [36]. The simulations depict an increase in temperature of about 1100 K and a 1 mol m^{-3} increase in O radical concentration, occurring in about 19 ns. In comparison, the original phenomenological model [24] required about 50 ns of characteristic pulse duration to impart the same amount of temperature and O density increase. Therefore, a very close agreement can be observed between the present results and experiments in terms of the characteristic pulse duration to achieve ultrafast gas heating and O_2 dissociation. Though both

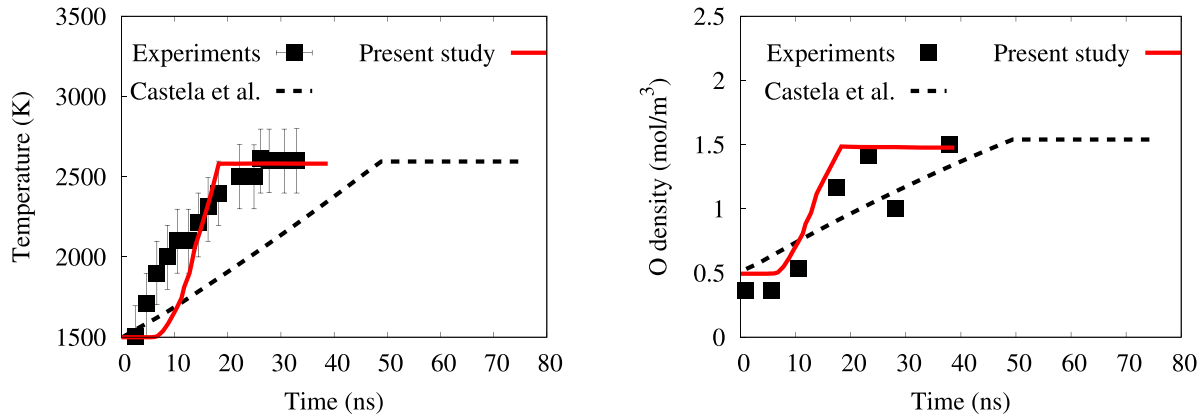

(a) Temperature (K) (b) O radical concentration (mol/m^3)

Figure 4. The evolution of (a) temperature (K) and (b) O radical concentration (mol m^{-3}), obtained using the improved phenomenological model (solid line), compared against the original phenomenological model (dashed lines) [24] and experiments (symbols) [36] for a single pulse discharge. The experimental uncertainties in temperature are ±200 K. The experiment, improved model, and the original phenomenological model all deposit 700 μJ energy during the pulse.

the current and the original model deposited ∼700 μJ of energy during the discharge pulse, the rise time in the present model is significantly closer to experiments (∼25 ns). Since the total energy deposition in both models does not differ, the improved accuracy of the present model can be attributed to the incorporation of a more precise spatiotemporal evolution of PPD as compared to the simplified distribution of PPD in the original model [24].

To ascertain the validity of the present model post-discharge, simulations are performed to predict the temporal evolution of the radii of the pressure wave (corresponding to the contour of peak pressure) and the heated channel (identified by the boundary defined at 1000 K) after the pulse. Figure 5 shows the evolution of pressure wave and heated channel radius using the improved phenomenological model (solid lines), compared against the original phenomenological model (dashed lines) [24] and the experiments [63] in the literature. A close agreement can be observed between the present model, the original model [24], and the experiments [63]. Nevertheless, it should be noted that the present model adhered to a pulse energy deposition of 1.5 mJ, the same as that of the experiment. In contrast, the original model had to downscale the energy deposition to about 0.8 mJ (about half the experimental value) to match the experimental evolution. Thus, the present model with spatiotemporal evolution of PPD is found to be able to predict the post-discharge dynamics of the pressure wave and the heated channel without the need for adjustments in the energy deposition.

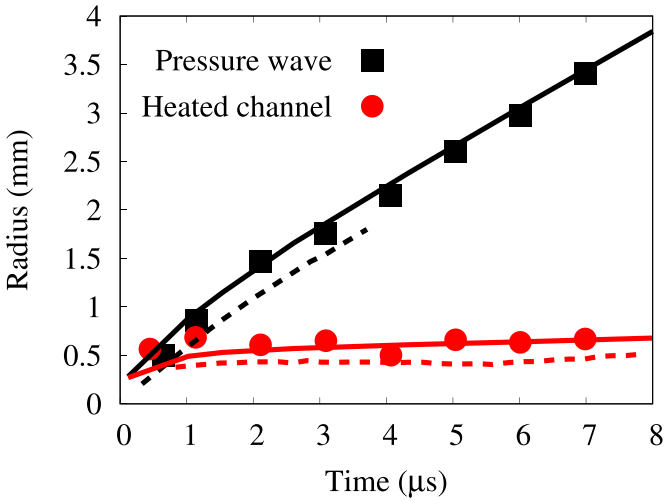

Figure 5. The evolution of radius of the pressure wave and heated channel post a single pulse discharge as obtained using the improved phenomenological model (solid line, 1.5 mJ energy deposited during the pulse), compared against the original phenomenological model (dashed lines, 0.8 mJ energy deposited during the pulse) [24] and experiments (symbols, 1.5 mJ energy deposited during the pulse) [63].

3.2. Streamer evolution at different gap distances

Upon validating against experiments [36, 63] and benchmarking against the original phenomenological model [24] to demonstrate improvements in prediction (see figures 4 and 5), the present work employs the improved phenomenological model to investigate the streamer evolution in a stoichiometric CH_4/air mixture between pin-to-pin electrodes, maintained initially at 300 K and 1 atm. Three different pin-to-pin configurations are investigated: 1 mm discharge gap with an applied voltage of 5 kV and pulse duration of 20 ns, 2 mm discharge gap with an applied voltage of 10 kV and pulse duration of 11 ns, and finally, 4 mm discharge gap with an applied voltage of 20 kV and pulse duration of 7 ns. The discharge gap lengths were selected to represent three conditions relative to the quenching distance [71] for a stoichiometric methane-air flame: below the quenching distance (1 mm), at the critical quenching distance (2 mm), and above the quenching distance (4 mm). The applied voltage is varied proportionally to the gap distance to maintain a similar average electric field (50 kV cm^{-1}) with an average reduced electric field (E/N) of

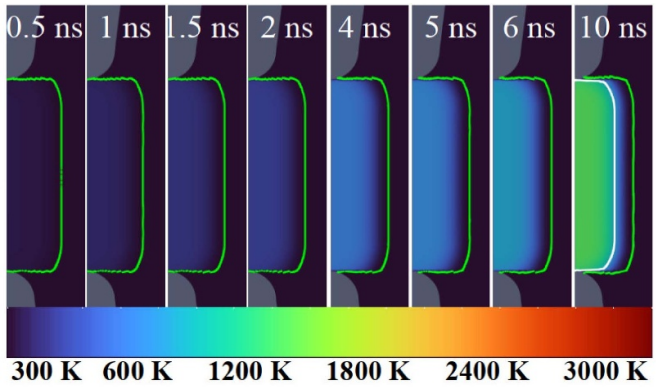

(a) Original model

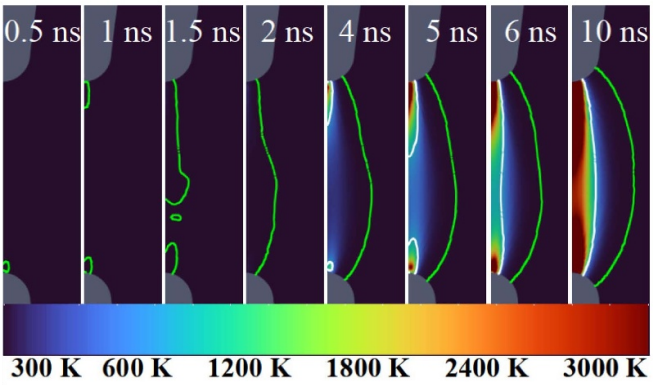

(b) Improved model with spatiotemporal plasma power density

Figure 6. The evolution of temperature during the pulse discharge from (a) the original model [24] and (b) the improved model incorporating spatiotemporal plasma power density for a 1 mm discharge gap and an applied voltage of 5 kV. The green line represents the propagation of the streamer (quantified by O mass fraction of 0.005), and the white line denotes the evolution of the hot kernel (quantified by 1000 K contour).

∼200 Td for the three discharge gaps. The energy deposited during the discharge for 1 mm, 2 mm, and 4 mm is limited to 1.5 mJ, 3 mJ, and 6 mJ, respectively to maintain similar average energy densities for the three discharge gaps.

Figure 6 illustrates the temperature evolution during the plasma discharge, as obtained using both the original model [24] and the improved model, which incorporates the spatiotemporal distribution of PPD, for a 1 mm discharge gap. The propagation of the hot zone, generated due to fast gas heating, is depicted by the white line, delineating a 1000 K isocontour. Initially, the original phenomenological model [24] portrayed a cylindrical and uniformly evolving temperature distribution extending beyond the electrode tips (as shown in figure 6(a)). However, the present model exhibits a preferential evolution of the temperature distribution. Hot zone formation is observed near the electrodes, gradually evolving towards the center of the discharge gap (as shown in figure 6(b)). While the original model exhibited an early rise in temperature distribution, hot zone formation (quantified by $T>1000$ K) was observed only around 10 ns. Conversely, the improved phenomenological model showed no significant temperature distribution until around 2 ns, but resulted in the early formation of comparatively smaller hot zones near the electrodes, around 3 ns, limited within a radial distance not exceeding the tip radius of the electrode, in contrast to the original model [24]. Despite their smaller size, the peak temperatures in the hot zones near electrodes obtained using the present model were significantly higher (∼8000 K) compared to the original model (∼1500 K). Such high temperatures can be attributed to localized heating near the electrodes induced by intense electric fields in the sheath regions [72] and the large current flows typical of NRP spark discharges [73], highlighting non-uniform energy deposition along the electrode gap. Despite the local gas temperature reaching 8000 K, the local electron temperature is significantly higher, attaining 18 eV (i.e. 208 881 K) locally near the electrode before streamer connection and approximately 4 eV (i.e. ∼46 418 K) after connection. Consequently, the plasma remains a non-equilibrium (although thermal/high-temperature) plasma, even at such elevated local gas temperatures due to strong plasma-induced local gas heating. This observed preferential spatiotemporal evolution of temperature in the improved model can be attributed to the incorporation of spatiotemporal PPD distribution obtained from detailed plasma simulations using PASSKEy [34]. As the phenomenological model populates the temperature distribution proportionally to that of the PPD (see equation (16)), the time-varying PPD distribution, evolving preferentially from the electrode tips towards the center of the discharge gap, is simply the cause of the observed temperature evolution in the improved model, as compared to the temporally invariant and spatially cylindrical PPD distribution in the original model [24].

Despite the temperature contours providing insights into the evolution of hot zones resulting from fast gas heating, they do not offer a comprehensive indication of how the streamer itself evolves. A more nuanced understanding of streamer propagation can be attained by quantifying the isocontour of O radical at a mass fraction of 0.005, delineated by the green lines in figure 6. This choice is substantiated by observed parallels in the spatiotemporal evolution of electron number density and O radical number density, as unveiled from the detailed plasma simulations conducted using PASSKEy [34] in the present work. This similarity has been illustrated in figure 7. The original phenomenological model [24] is found to render an almost cylindrical and invariant contour of the streamer, both spatially and temporally (see figure 6(a)). Moreover, the streamer is observed to be present from the earliest instance of plasma discharge itself (0.5 ns), and its structure remains unchanged throughout the plasma discharge. Although the streamer depicted by the present study exhibited a cylindrical shape and the radius of this streamer (quantified by O radicals) was similar to the original model [24] at 10 ns (about 0.27 mm), the radial extent of the temperature-based cylindrical body was about 50% smaller (about 0.135 mm) compared to the predictions from the original model (about 0.21 mm) [24]. This indicates the tendency of the original model to overpredict the discharge kernel (recall section 3.1), where an energy downscaling was required in the original model [24] to match experiments [63]. This observation emphasizes the inadequacy of the original phenomenological model [24] in capturing the formation of the

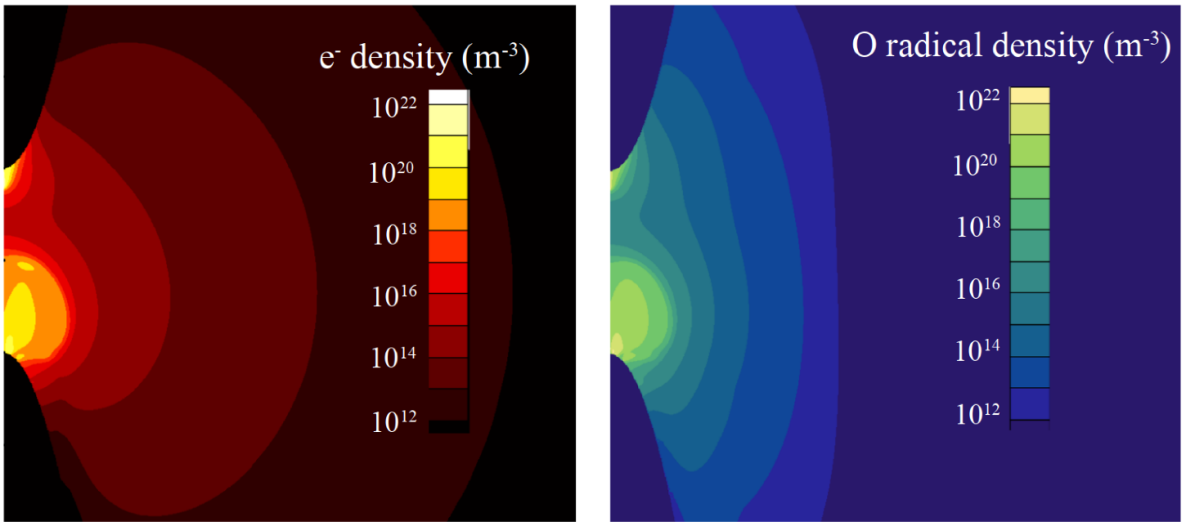

(a) Electron density (m^{-3}) (b) O radical density (m^{-3})

Figure 7. The contours of (a) electron number density (m^{-3}) and (b) O radical density (PPD, $W m^{-3}$) at 1 ns as obtained using 2D axisymmetric plasma fluid simulations using PASSKEy [34].

streamer head, its propagation towards the center of the discharge gap, and the subsequent connection of streamer heads. In contrast, the improved phenomenological model from the present investigation renders a spatiotemporally evolving isocontour of O radical with a clear initiation near the electrodes at 0.5 ns, followed by propagation towards the discharge center, and the subsequent connection of the opposing isocontours at approximately 2 ns, forming a channel (see figure 6(b)). Post-connection, the channel formed due to the connection of opposing isocontours enlarges with time and adopts an ellipsoidal structure by around 10 ns, as opposed to the cylindrical structure in the original model. This evolution mirrors the dynamics of the streamer head from initiation to connection and further enlargement of the conducting channel with additional energy in the discharge. The improved phenomenological model from the present investigation achieves this by incorporating a more accurate representation of the underlying physical processes, particularly by accounting for the spatiotemporal evolution of PPD from detailed plasma simulations using PASSKEy [34], thereby facilitating a more accurate evolution of O radical isocontours. The accurate implementation of streamer evolution, facilitated by the improved phenomenological model is crucial in plasma discharges within fuel-air mixtures. Unlike a simplistic cylindrical plasma channel in the original model [24], an accurate representation of streamer dynamics (see figures 4 and 5 observing the accuracy of streamer and kernel dynamics) is essential for predicting ignition events accurately. The shape of the streamer can affect ignition and quenching events [74, 75], and inaccuracies in its representation may lead to either over-prediction or under-prediction of these critical events in a combustible gas mixture.

The influence of discharge gap size on streamer dynamics is investigated using detailed simulations employing PASSKEy [34], as well as using the improved and original phenomenological model [24]. Specifically, discharge gaps of 1 mm, 2 mm, and 4 mm are examined to understand their impact on streamer behavior. Detailed simulations in PASSKEy provide insights into the evolution of electron number density within the discharge gap, while the improved and original phenomenological model offers predictions regarding the evolution of O radical density. Figure 8 illustrates the evolution of electron number density in $\#/m^3$ (figures 8(a)–(c)) and the O radical number density in $\#/m^3$ from the present (figures 8(d)–(f)) and original phenomenological models (figures 8(g)–(i)) along the discharge axis for discharge gaps of 1 mm (5 kV), 2 mm (10 kV), and 4 mm (20 kV). The streamer head formation and propagation commence at sub-nanosecond timescales for all discharge gaps, as observed in the evolution of electron number density obtained from detailed simulations (figures 8(a)–(c)). The streamer heads, represented by electron-rich peaks on either side (figures 8(a)–(c)), proceed to connect at approximately 1.5 ns for the 1 mm discharge gap. With an increase in the gap distance to 2 mm, a faster connection is observed occurring at around 1 ns. Further increasing the gap distance to 4 mm also demonstrates the connection occurring at sub-nanosecond timescales. For the 1 mm discharge gap, the negative streamer head, depicted by the electron peak near the cathode (i.e. the left-most location in the discharge gap in figure 8), propagates faster in time compared to the positive streamer head, depicted by the electron peak near the anode (i.e. right-most location in the discharge gap in figure 8). As a result, both streamer heads connect closer to the anode, as shown in figure 8). However, for both the 2 mm and 4 mm gaps (figures 8(b) and (c)), the propagation velocity of the positive streamer head is found to increase, leading to the connection of streamer heads occurring closer to the discharge center. With the linear increase in applied voltage with increasing gap distance, the average applied electric field remains the same for all three discharge gaps and hence cannot solely explain the aforementioned observation. However,

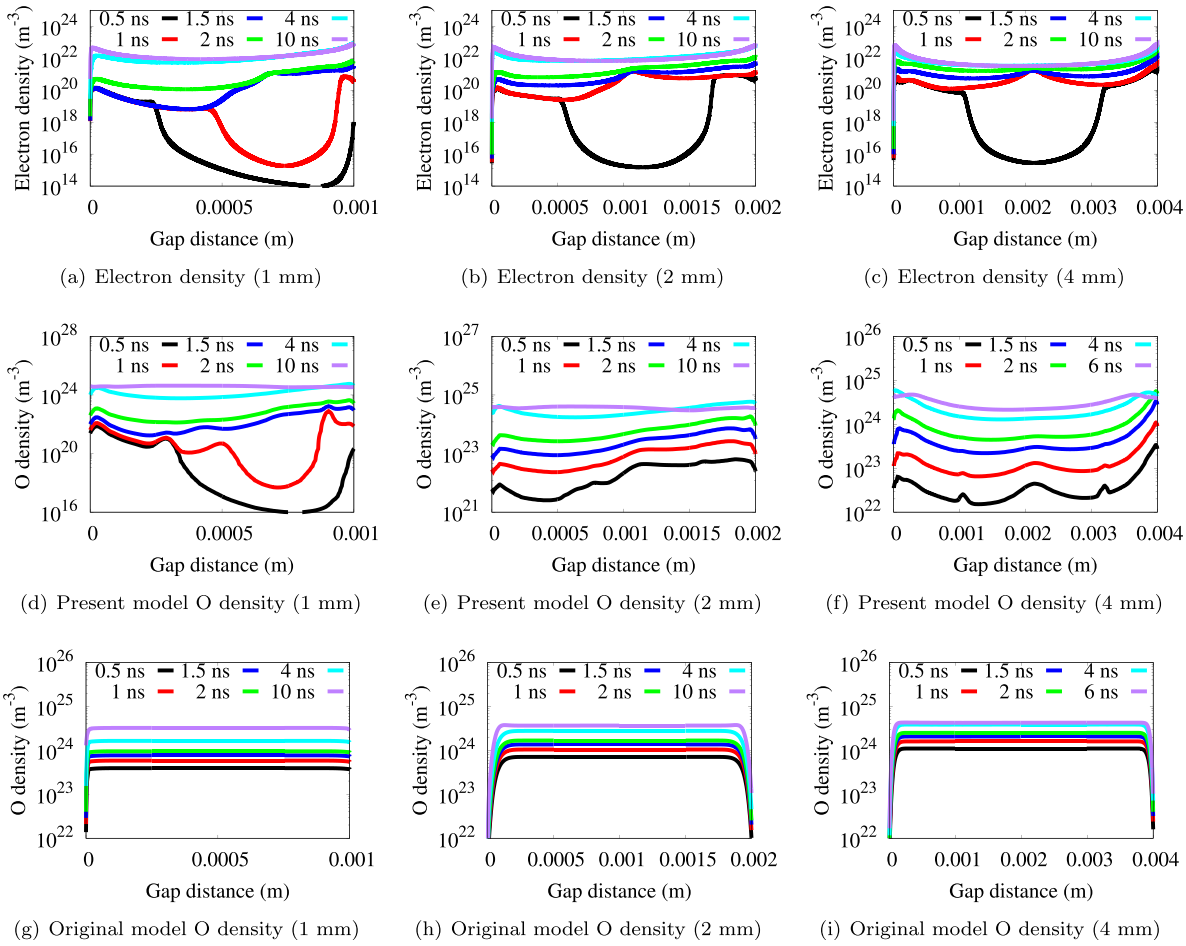

(a) Electron density (1 mm) (b) Electron density (2 mm) (c) Electron density (4 mm)

(d) Present model O density (1 mm) (e) Present model O density (2 mm) (f) Present model O density (4 mm)

(g) Original model O density (1 mm) (h) Original model O density (2 mm) (i) Original model O density (4 mm)

Figure 8. The evolution of (a)–(c) electron number density in $\#/m^3$, (d)–(f) O radical number density in $\#/m^3$ from the present model and, (g)–(i) O radical number density in $\#/m^3$ from the original model [24], along the discharge axis for 1 mm (5 kV), 2 mm (10 kV), and 4 mm (20 kV) discharge gaps.

since the same electrode geometry was used for all three cases without adjusting the radius of curvature, there is a larger initial local electric field near the electrode for larger gap distances, as shown in figure 9. Given that streamer initiation and propagation depend on local electric field values, configurations with a larger local electric field near the electrode tip (e.g. 4 mm) lead to faster initiation and propagation of streamers.

Comparing the outcomes from the present and original phenomenological models with those derived from detailed plasma simulations (discussed earlier) elucidates the predictive capability of the present phenomenological model. In particular, we analyze the evolution of O radical density along the discharge axis for discharge gap sizes of 1 mm, 2 mm, and 4 mm, as obtained using the improved phenomenological model (figures 8(d)–(f)) and the original phenomenological model (figures 8(g)–(i)). For the 1 mm discharge gap, O radical predictions from the improved phenomenological model (figure 8(d)) exhibit a closer agreement with the evolution of electron density (figure 8(e)). The O density displays two peaks at either electrode end at earlier time scales ($<$1.5 ns), followed by the connection of these peaks at 1.5 ns and further evolution towards a higher uniform O density across the discharge, mirroring the behavior observed in the electron density (figure 8(a)). While a clear distinction between the two O radical peaks is not observed at either electrode end for the 2 mm and 4 mm gaps, the profiles still demonstrate a preferential rise towards the electrode ends for $<$ 1 ns, followed by a steady increase towards a uniform O density distribution (see figures 8(e) and f)). These observations in the O radical evolution obtained using the improved phenomenological model are notably different when compared to the O density evolution obtained using the original phenomenological model [24] (figures 8(g)–(i)), where the O density sharply drops to zero infinitesimally closer to the electrode tip and remains uniformly distributed across the discharge. Moreover, the temporal evolution appears to be highly linear in the original phenomenological model compared to the present work. These findings, along with the comparison of the predictions of the present and original phenomenological model [24] to the detailed plasma simulations [34], highlight the fidelity of the improved phenomenological model.

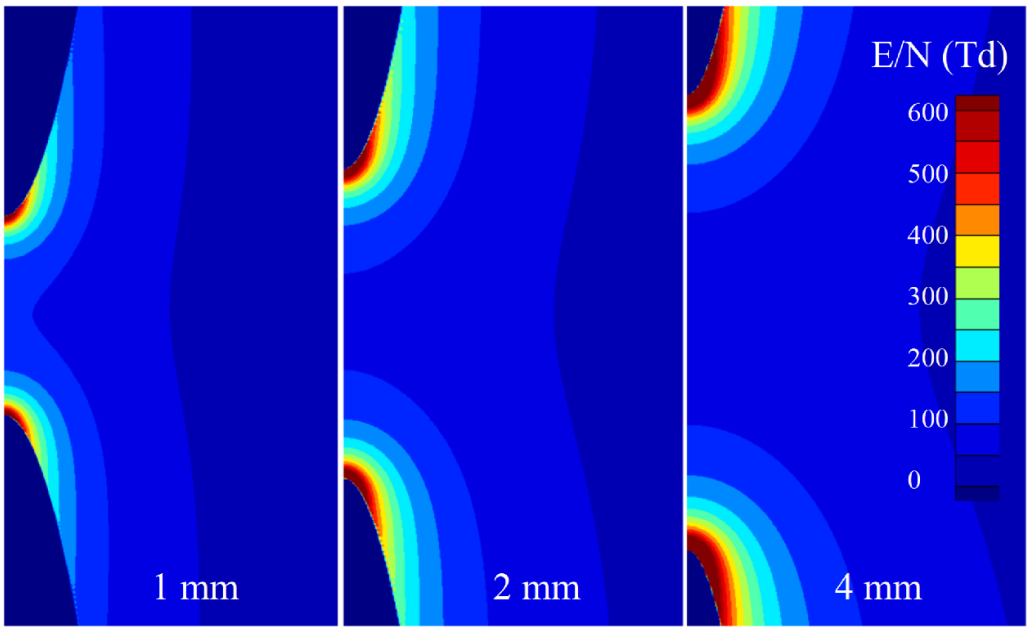

Figure 9. The contours of initial reduced electric field (E/N) at $t = 0$ for (a) 1 mm (5 kV), (b) 2 mm (10 kV), and (c) 4 mm (20 kV) discharge gap obtained from the detailed plasma simulations in the present study.

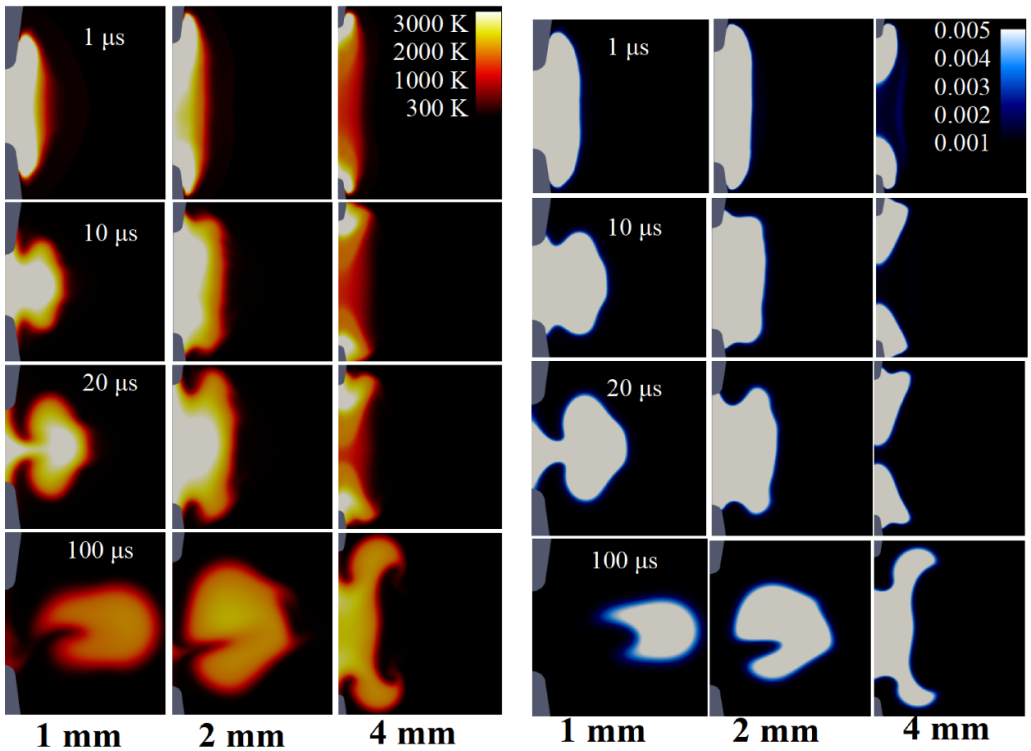

(a) Temperature (b) OH mass fraction

Figure 10. The evolution of (a) temperature and (b) OH mass fraction for a 1 mm (5 kV), 2 mm (10 kV), and 4 mm (20 kV) discharge gap obtained from the improved phenomenological model.

The examination of post-discharge ignition kernel evolution across three distinct electrode configurations is facilitated through the application of the improved phenomenological model presented in this study. Figure 10 illustrates the post-plasma discharge evolution of temperature and OH mass fraction for electrode configurations of 1 mm, 2 mm, and 4 mm. Across all scenarios, at 1 μs post-discharge, a high-temperature region rich in OH (i.e. ignition kernel) is observed close to the electrodes, with the temperature and OH mass fraction at the discharge center diminishing as the discharge

gap increases. By 10 μs, the ignition kernel begins to assume different shapes: toroidal but attached to electrodes for the 1 mm configuration, cylindrical for the 2 mm, and dumbbell-shaped for the 4 mm. Advancing to 20 μs propagates the ignition kernel further, and by 100 μs, a distinctly separated toroidal kernel is evident for both 1 mm and 2 mm configurations, while the ignition kernel remains attached for the 4 mm configuration. Although both kernels are separated by this time, the ignition kernel in the 2 mm case is notably closer to the electrodes and larger compared to the ignition kernel in the 1 mm discharge gap. The increase in the size of the ignition kernel with gap distance can be simply attributed to the deposition of the same energy density across larger discharge volumes for the larger discharge gaps. In essence, the ignition kernels for the 1 mm and 2 mm cases appear as a single large, cylindrical kernel that expands radially outward due to the two high-temperature zones near the two electrodes being close. For the 4 mm gap distance, the two hot zones near the two electrodes are significantly farther apart initially, and the initial gas temperature at the center of the discharge gap is considerably lower, leading to a spherical expansion of two separate kernels from the electrode tips that eventually merge and later expand radially outward as a single large kernel.

3.3. *Interactions of successive ignition kernels*

The subsequent analysis is directed towards elucidating the interactions between ignition kernels arising from consecutive plasma discharges. The improved model from the present investigation is employed to simulate NRP discharges across the three gap distances. In these simulations, a second pulse is initiated after 100 μs from the first pulse, corresponding to a pulse repetition frequency of 10 kHz, with the respective PPD distribution employed for each electrode configuration. The selection of a repetition frequency of 10 kHz is deliberate, aiming to allow sufficient time for the propagation of the ignition kernel generated by the initial discharge. This duration enables the discharge gap to partially revert back to its original thermochemical state, particularly for the 1 mm and 2 mm gaps, as depicted in figure 10. Although the 4 mm gap does not fully return to its original thermochemical state, the region closer to the electrode tips exhibits a closer resemblance. Furthermore, the proximity of the ignition kernel to the electrode tips at earlier times post-discharge, as illustrated in figure 10, justifies the choice of a 10 kHz repetition frequency.

Figure 11 depicts the evolution of temperature (red-yellow contours) overlaid with OH mass fraction (white-blue contours) for discharge gaps of 1 mm, 2 mm, and 4 mm, as derived from the improved phenomenological model. The OH mass fraction contours, defined for mass fractions $\geqslant 0.001$, highlight the ignition kernel. In the case of the 1 mm gap, the second discharge distinctly separates from the preceding ignition kernel at the earliest instance post-second discharge (0.1 μs). Conversely, for the 2 mm gap, the second discharge initially interacts with the previous ignition kernel (0.1 μs), albeit superficially at the kernel boundary. By contrast, the second discharge fully interacts and merges with the previous ignition kernel at an early stage (0.1 μs). By 10 μs, the ignition kernel due to the second discharge destructively interferes with the prior one, quenching reactive regions (as indicated by the OH contours). This interference results from the initial disconnect between the ignition kernels, with the second kernel expanding towards the first, thereby compressing the fresh gas mixture into the first kernel, and diminishing the reactive region. In the case of the 2 mm gap, the first and second ignition kernels commence interaction early on (0.1 μs), expanding together by 10 μs, with no flow of fresh gas mixture to bifurcate the first kernel. By 50 μs, the first kernel is entirely quenched, while the second kernel assumes a cylindrical shape for the 1 mm gap. Meanwhile, the combined first and second kernels form a larger, separated ignition kernel that remains detached from the electrodes for the 2 mm discharge gap. Subsequently, at 0.5 ms, the ignition kernel continues to grow detached for the 2 mm gap, while for the 1 mm gap, the kernel remains attached and shows limited expansion. In comparison to 1 mm and 2 mm, the second and first kernels in the 4 mm discharge gap consistently combine and expand, remaining attached to the electrodes throughout.

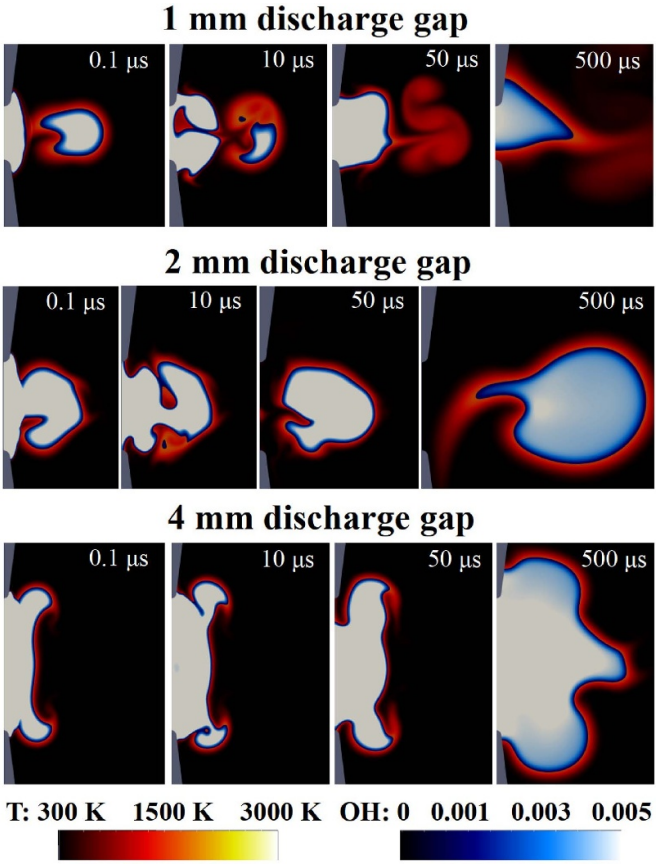

Figure 11. The spatiotemporal evolution of temperature (red-yellow contours) overlaid with the isocontour of OH mass fraction (white-blue contours), defined for OH mass fraction $\geqslant 0.001$ post second pulse for 1 mm (5 kV), 2 mm (10 kV), and 4 mm (20 kV) discharge gaps, obtained from the improved phenomenological model.

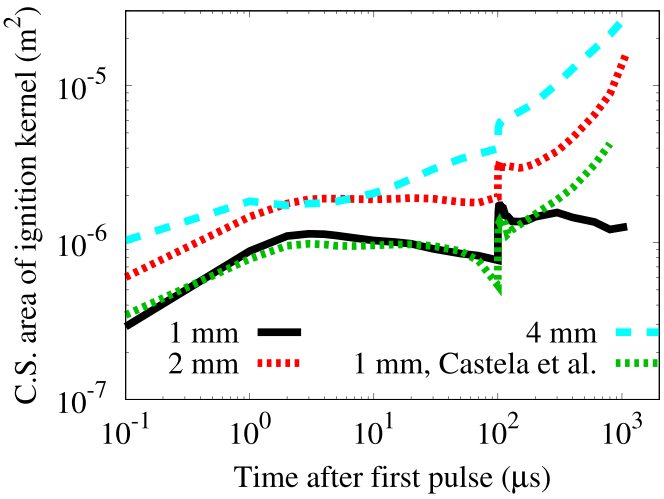

Figure 12. Evolution of the cross-sectional area of the ignition kernel obtained from the iso-surfaces of OH mass fraction (quantified by a mass fraction $\geqslant 0.001$) for 1 mm, 2 mm, and 4 mm gap discharges for the present study along with that from the original model [24] for 1 mm.

Additionally, figure 12 exhibits the evolution of the cross-sectional area of the ignition kernel obtained from the iso-surfaces of OH mass fraction (as quantified by a mass fraction $\geqslant 0.001$) for 1 mm, 2 mm, and 4 mm gap discharges. The evolution is depicted from 0.1 μs after the first discharge until 1 ms post-second discharge, providing a comprehensive view of the ignition kernel's behavior. Following the initial discharge, the ignition kernel area experiences expansion, reaching its peak size within the first few microseconds for both 1 mm and 2 mm gaps, and within the first microsecond for the 4 mm gap. Subsequently, for the 1 mm gap discharge, the ignition kernel area exhibits a decline from its peak value of approximately 1×10^{-6}m^2 to about 7×10^{-7}m^2 before the onset of the second discharge. This reduction can be attributed to the early attempt at toroidal kernel separation and the formation of lobes on the kernel caused by the outward pushing and stretching of the ignition kernel. Conversely, for the 2 mm gap discharge, the ignition kernel area remains relatively stable, hovering around the peak value of approximately 2×10^{-6}m^2 until the start of the second discharge. This stability may be attributed to the delayed separation and the maintenance of a relatively cylindrical shape for the kernel, thereby mitigating the intensity of stretching and lobe formations. In contrast to the 1 mm and 2 mm gap discharges, the ignition kernel area for the 4 mm gap remains at its peak value of approximately 2×10^{-6}m^2 for only about 1 μs post-initial rise, before continuing to increase until the next pulse. At 100 μs, an instantaneous spike in the cross-sectional area of the ignition kernel is observed for all three configurations, indicative of the second pulse discharge. Following the second pulse, the behavior of the ignition kernel displays fluctuations, suggesting the quenching of the first kernel while the second kernel expands for the 1 mm configuration. However, for the 2 mm and 4 mm gaps, the ignition kernels undergo rapid expansion, indicative of successful ignition events. The cross-sectional area of the ignition kernel post-second discharge is observed to increase with the discharge gap distance, which is similar to the experimental observations at similar repetitive frequencies [76]. Figure 12 also shows the evolution of the cross-sectional area of the ignition kernel for 1 mm as obtained using the original phenomenological model [24] for the same deposited pulse energy (1.5 mJ) of 1 mm (green dotted line). It can be observed that the ignition kernel obtained from the original model [24] closely follows the present model up to the second pulse, post which a rapid increase in the cross-sectional area is observed depicting an early ignition. This observation signifies the variation of post-discharge ignition kernel prediction with and without the implementation of spatiotemporal PPD.

3.4. *Effect of turbulence on kernel propagation*

Finally, the evolution of the ignition kernel generated by the nanosecond plasma pulses is investigated under homogeneous isotropic turbulent (HIT) velocity fields, as is also done in references [24, 28], although in 2D domains. 3D HIT solutions using Rogallo's approach [77] are obtained to ensure divergence-free and real-valued velocity vectors. These conditions are given in equation (23), where $\vec{k}$ is the wave number vector and $\vec{\hat{u}}$ is the Fourier-transformed velocity vector in the wave number space.

$$\begin{aligned} \vec{k} \cdot \vec{\hat{u}} &= 0; \\ \hat{u}_i\left(\vec{k}\right) &= \hat{u}_i^*\left(-\vec{k}\right). \end{aligned} \tag{23}$$

The initial condition imposed on $\vec{\hat{u}}$ is given by:

$$\vec{\hat{u}} = \left(\frac{\alpha k k_1 + \beta k_1 k_3}{k\sqrt{k_1^2 + k_2^2}}\right)\hat{e_1} + \left(\frac{\beta k_2 k_3 - \alpha k k_1}{k\sqrt{k_1^2 + k_2^2}}\right)\hat{e_2} + \left(\frac{\beta\sqrt{k_1^2 + k_2^2}}{k}\right)\hat{e_3}, \tag{24}$$

where k_1, k_2 and k_3 are the components of the wave-number vector in the three directions and $k = \sqrt{k_1^2 + k_2^2 + k_3^2}$. α and β are given in equations (25) and (26).

$$\alpha(k) = \sqrt{\frac{E(k)}{4\pi k^2}}\exp(j\theta_1)\cos\phi; \tag{25}$$

$$\beta(k) = \sqrt{\frac{E(k)}{4\pi k^2}}\exp(j\theta_2)\sin\phi. \tag{26}$$

Here, θ_1, θ_2 and ϕ are random numbers between 0 and 2π, and $E(k)$ is the turbulent kinetic energy per unit mass in the wave-number space, assumed to follow the Passot-Pouquet spectrum [78] given in equation (27).

$$E(k) = 16\sqrt{\frac{2}{\pi}}\frac{u_0^2}{k_0}\left(\frac{k}{k_0}\right)^4 \exp\left(-2\left(\frac{k}{k_0}\right)^2\right). \tag{27}$$

In the above equations, k_0 is the wave number of the most energetic eddies, and u_0 is the RMS velocity. The length scale corresponding to k_0 should be smaller than the integral length

scale, which is typically chosen to be a quarter of the domain size to avoid the interference of the boundary conditions on the largest eddy that can be resolved. In this simulation, we fix k_0 to be 10 and use two sets of turbulent Reynolds numbers (Re_τ) of 50 and 500. The selection of Re_τ in this study was made to maintain proximity to the original values of 44 and 395 from the previous investigation by Castela *et al* [24], while adjusting them to be exactly one order of magnitude apart for consistency and comparability. The corresponding RMS velocities are 5 $\mathrm{m\,s^{-1}}$ and 10 $\mathrm{m\,s^{-1}}$ respectively. The kinetic energy spectrum $E(k)$ follows, $\int_0^\infty E(k)\mathrm{d}k = 3u_0^2/2$. This synthetic initial condition for velocity is generated without considering the medium viscosity. However, the viscosity eventually acts in the DNS to determine the turbulence cascade and interaction with the chemistry.

Since the domain used in the DNS is an octant sector of a cylinder, the HIT initial conditions are interpolated to this domain from a cubical domain with a side length equal to the diameter of the cylindrical octant sector (12 mm). Figure 13 portrays the evolution of temperature overlaid with the isocontours of OH corresponding to a mass fraction $\geqslant 0.001$ for the discharge gaps of 1 mm with HIT corresponding to (a) $k_0 = 15\,\mathrm{m^{-1}}, u_0 = 5\,\mathrm{m\,s^{-1}}$ and (b) $k_0 = 15\,\mathrm{m^{-1}}, u_0 = 10\,\mathrm{m\,s^{-1}}$, as derived from the improved phenomenological model. For the brevity of the present work, the effect of turbulence is investigated only using 1 mm discharge gap configurations. Figure 13 initially shows the ignition kernel formed after the first pulse at an instance just before the second pulse. For both RMS velocities of 5 and 10 $\mathrm{m\,s^{-1}}$, it can be observed that the ignition kernel is still detached from the electrodes, albeit much smaller in size compared to the original ignition kernel in the absence of HIT at 100 μs (see figure 11). The ignition kernel is found to be smaller for $u_0 = 10\,\mathrm{m\,s^{-1}}$ and closer to the electrodes when compared to 5 $\mathrm{m\,s^{-1}}$. After the second pulse, the ignition kernel for $u_0 = 5\,\mathrm{m\,s^{-1}}$ (see figure 13(a)) evolves similarly to that of the quiescent mixture up to around 10 μs as shown in figure 11. Beyond the 10 μs, the two kernels continue to exist separately, unlike the quiescent case where the earliest ignition kernel is completely quenched around the 50 μs mark. Despite the survival of the first kernel from the destructive quenching due to the expansion of the second kernel, both ignition kernels are observed to quench subsequently at later time stages ($\sim$ 100 μs) when compared to the quiescent ignition kernel. A similar behavior can be observed for $u_0 = 10\,\mathrm{m\,s^{-1}}$ (see figure 13(b)). Both the cases with HIT, when compared against the quiescent ignition kernel evolution (figure 11), are observed to exhibit rather elongated hot zones and OH contours at 10 μs, with the $u_0 = 10$ $\mathrm{m\,s^{-1}}$ exhibiting a more elongated and dissipated hot zone compared to $u_0 = 5\,\mathrm{m\,s^{-1}}$. This can be attributed to the turbulent mixing, enabling enhanced radical and heat losses of hot zones as observed in Taneja and Yang [28].

To delineate the differences in the evolution of ignition kernels between the two turbulent intensities corresponding to $u_0 = 5$ $\mathrm{m\,s^{-1}}$ and 10 $\mathrm{m\,s^{-1}}$, the present study investigates the evolution of the cross-sectional area of the ignition kernel as shown in figure 14, derived from the iso-surfaces of

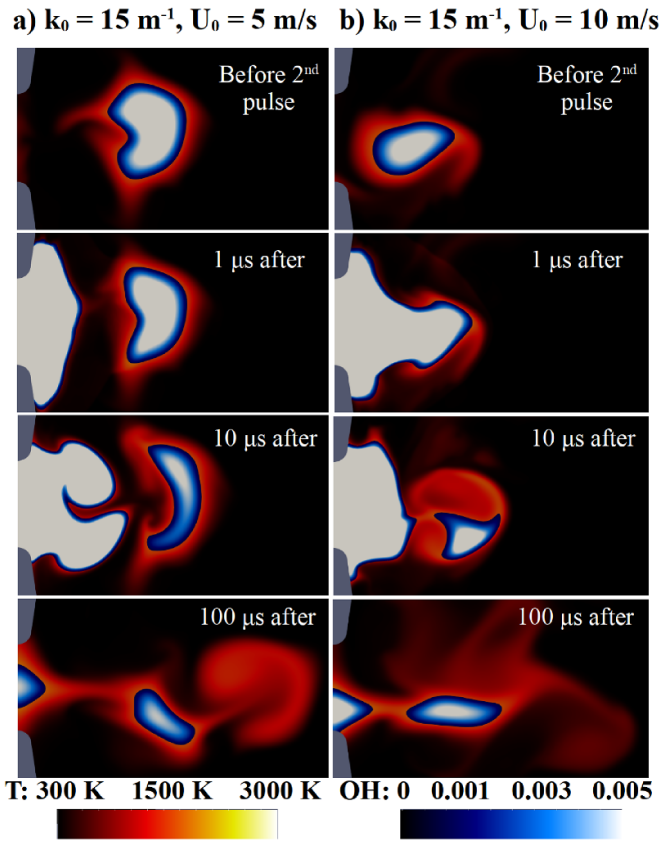

Figure 13. The evolution of temperature (red-yellow region) overlaid with the isocontours of OH mass fraction (blue-white contour, defined for OH mass fraction $\geqslant 0.001$) for a 1 mm discharge gap (5 kV) with homogeneous isotropic turbulence (HIT) corresponding to (a) $k_0 = 15\,\mathrm{m^{-1}}, u_0 = 5\,\mathrm{m\,s^{-1}}$ and (b) $k_0 = 15\,\mathrm{m^{-1}}, u_0 = 10\,\mathrm{m\,s^{-1}}$, as obtained from the improved phenomenological model.

OH mass fraction presented earlier in figure 13. The cross-sectional area of the ignition kernel for the two HIT cases (dashed and dotted lines) is compared against that of the quiescent kernel evolution (solid line). Initially, all three cases exhibit similar evolution patterns up to the first few microseconds after the first pulse. However, as time progresses, the two HIT cases experience a reduction in the area of the ignition kernel, with the kernel corresponding to the highest turbulent intensity ($u_0 = 10$ $\mathrm{m\,s^{-1}}$) exhibiting a notably steeper reduction in size. Following the second pulse, the ignition kernel corresponding to $u_0 = 5\,\mathrm{m\,s^{-1}}$ maintains its size initially after the discharge, closely following the quiescent ignition kernel up to 70 μs. However, after this point, it quickly quenches. In contrast, the ignition kernel corresponding to $u_0 = 10\,\mathrm{m\,s^{-1}}$ quenches immediately after the second pulse. This discrepancy can be attributed to the difference in turbulent timescales, with the case corresponding to $u_0 = 10\,\mathrm{m\,s^{-1}}$ experiencing faster turbulent mixing and convection, thereby leading to pronounced quenching. Therefore, turbulence fosters ignition quenching, with higher-intensity turbulence notably hastening the quenching process of the ignition kernel.

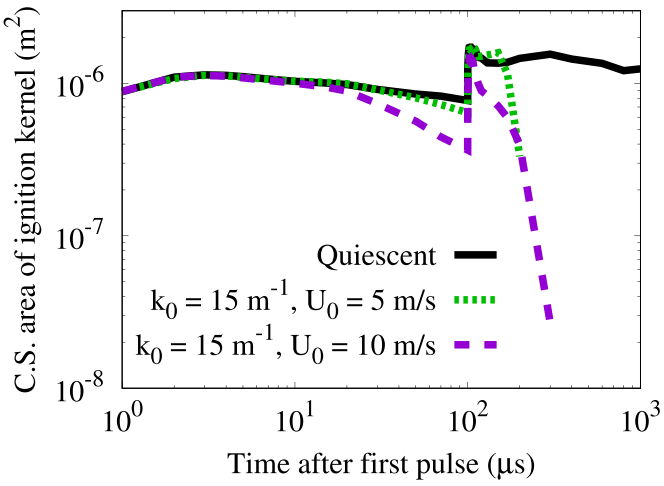

Figure 14. The evolution of the cross-sectional area of the ignition kernel obtained from the iso-surfaces of OH mass fraction (quantified by a mass fraction $\geqslant 0.001$) for a 1 mm discharge gap (5 kV) in quiescent (black solid line) and turbulent mixtures ($k_0 = 15\,\mathrm{m}^{-1}, u_0 = 5\,\mathrm{m\,s}^{-1}$—green dotted line; $k_0 = 15\,\mathrm{m}^{-1}$, $u_0 = 10\,\mathrm{m\,s}^{-1}$—violet dashed line).

4. Conclusion

An investigation into nanosecond plasma discharges in atmospheric-pressure stoichiometric methane-air mixtures has been undertaken, encompassing both quiescent and turbulent scenarios. An improved phenomenological model based on the existing model in the literature [24, 28], refined to capture the nonlinear evolution of plasma discharge, serves as the basis of this work. The enhancement involved integrating a detailed spatiotemporal evolution of PPD, derived from comprehensive plasma simulations [34], into the existing phenomenological model [28]. The improved model was subsequently validated against experimental data [36], demonstrating improved accuracy in predicting ultrafast gas heating and O_2 dissociation during plasma discharge, compared to the original model in the literature [24, 28]. In addition, the model exhibited close agreement with the experimental pressure wave and heated channel profiles [38] without the need to tune the energy deposition, when compared to the original model in the literature [24].

Subsequently, the enhanced phenomenological model has been employed to assess the evolution of ignition kernels in atmospheric-pressure stoichiometric methane-air plasma discharges across various discharge gap configurations. Firstly, investigations using detailed plasma model [34] and improved phenomenological model reveal a non-uniform evolution of temperature and streamer distribution, originating from the electrode tips and progressing towards the discharge center, contrasting with the uniform cylindrical discharge described in the original phenomenological model [24]. Detailed plasma simulations highlight faster streamer propagation with larger discharge gaps (2 mm and 4 mm) when maintained at a similar average electric field, with the improved phenomenological model demonstrating closer agreement with the detailed plasma simulation upon comparing the O radical density evolution to electron density profiles. The evolution of post-discharge ignition kernels exhibits distinctive variations in shape and location, influenced primarily by the gap distance. Specifically, smaller gap discharges (1 and 2 mm) tend to yield separated toroidal kernels, while the larger gap (4 mm) results in attached and more cylindrical kernels.

Further, the improved phenomenological model has been employed to study interactions between successive ignition kernels resulting from consecutive plasma discharges across various gap distances. In the smallest gap (1 mm), the second discharge separates from the previous ignition kernel early on, while in the intermediate gap (2 mm), initial interaction occurs at the kernel boundary. However, in the widest gap (4 mm), ignition kernels consistently combine and expand, remaining attached to the electrodes. Early interaction in the smallest gap leads to a decline in kernel area before the second discharge, while delayed separation in the intermediate gap maintains a stable kernel area until the second discharge. The widest gap exhibits rapid expansion post-initial rise, indicating successful ignition events. Additionally, the model has been used to explore the impact of turbulence on ignition kernel evolution, revealing that under HIT, ignition kernels persist but are smaller and detached from electrodes. Despite surviving initial quenching, they are observed to eventually quench around 100 μs, suggesting that turbulent mixing enhances radical and heat losses from the ignition kernels, leading to elongated hot zones, particularly noticeable with higher turbulent intensity.

In conclusion, this study represents a significant step forward in refining phenomenological models for PAC, aiming for better accuracy. These advancements are pivotal for numerically investigating real-world PAC systems, to propel their utility in practical applications.

Data availability statement

The data cannot be made publicly available upon publication because no suitable repository exists for hosting data in this field of study. The data that support the findings of this study are available upon reasonable request from the authors.

Acknowledgment

The information, data, or work presented herein was funded in part by the Advanced Research Projects Agency-Energy (ARPA-E), U.S. Department of Energy, under Award Number DE-AR0001529, and in part by the National Science Foundation (NSF) under Award Number CBET 2002635. The views and opinions of authors expressed herein do not necessarily state or reflect those of the United States Government or any agency thereof. T S Taneja acknowledges the grant support from the NSF INTERN Supplemental Funding Opportunity and the University of Minnesota (UMN) Doctoral Dissertation Fellowship (DDF). The authors also acknowledge the Minnesota Supercomputing Institute (MSI) for its computational resources.

ORCID iD

Suo Yang https://orcid.org/0000-0002-9924-2645

References

[1] Starikovskaia S M 2006 *J. Phys. D: Appl. Phys.* **39** R265
[2] Ombrello T, Qin X, Ju Y, Gutsol A, Fridman A and Carter C 2006 *AIAA J.* **44** 142–50
[3] Starikovskiy A and Aleksandrov N 2013 *Prog. Energy Combust. Sci.* **39** 61–110
[4] Petitpas G, Rollier J D, Darmon A, Gonzalez-Aguilar J, Metkemeijer R and Fulcheri L 2007 *Int. J. Hydrog. Energy* **32** 2848–67
[5] Kim W, Mungal M G and Cappelli M A 2010 *Combust. Flame* **157** 374–83
[6] Regulations for emissions from vehicles and engines (available at: www.epa.gov/regulations-emissions-vehicles-and-engines)
[7] Road transport: reducing co emissions from vehicles (available at: https://climate.ec.europa.eu/eu-action/transport/road-transport-reducing-co2-emissions-vehicles_en#tab-0-0)
[8] Sun W, Uddi M, Won S H, Ombrello T, Carter C and Ju Y 2012 *Combust. Flame* **159** 221–9
[9] Lotfalipour R, Ghorbanzadeh A and Mahdian A 2014 *J. Phys. D: Appl. Phys.* **47** 365201
[10] Kimura I, Aoki H and Kato M 1981 *Combust. Flame* **42** 297–305
[11] Starikovskii A Y 2005 *Proc. Combust. Inst.* **30** 2405–17
[12] Kim Y, Stange S M, Rosocha L A and Ferreri V W 2005 *J. Adv. Oxid. Technol.* **8** 188–92
[13] Cha M S, Lee S, Kim K and Chung S H 2005 *Combust. Flame* **141** 438–47
[14] Leonov S B, Yarantsev D A, Napartovich A P and Kochetov I V 2006 *IEEE Trans. Plasma Sci.* **34** 2514–25
[15] Lou G, Bao A, Nishihara M, Keshav S, Utkin Y G, Rich J W, Lempert W R and Adamovich I V 2007 *Proc. Combust. Inst.* **31** 3327–34
[16] Kushner M J 2009 *J. Phys. D: Appl. Phys.* **42** 194013
[17] Ju Y and Sun W 2015 *Prog. Energy Combust. Sci.* **48** 21–83
[18] Starikovskaia S 2014 *J. Phys. D: Appl. Phys.* **47** 353001
[19] Mao X, Rousso A, Chen Q and Ju Y 2019 *Proc. Combust. Inst.* **37** 5545–52
[20] Taneja T S, Johnson P N and Yang S 2022 *Combust. Flame* **245** 112327
[21] Hagelaar G and Pitchford L C 2005 *Plasma Sources Sci. Technol.* **14** 722
[22] Scapinello M, Delikonstantis E and Stefanidis G D 2017 *Chem. Eng. Process.* **117** 120–40
[23] Johnson P N, Taneja T S and Yang S 2023 *Combust. Flame* **255** 112927
[24] Castela M, Fiorina B, Coussement A, Gicquel O, Darabiha N and Laux C O 2016 *Combust. Flame* **166** 133–47
[25] Matyash K, Schneider R, Taccogna F, Hatayama A, Longo S, Capitelli M, Tskhakaya D and Bronold F 2007 *Contrib. Plasma Phys.* **47** 595–634
[26] Abdollahzadeh M, Pascoa J and Oliveira P 2016 *Comput. Fluids* **128** 77–90
[27] Verma A K and Venkattraman A 2021 *Comput. Phys. Commun.* **263** 107855
[28] Taneja T S and Yang S 2022 Comparing low-mach and fully-compressible cfd solvers for phenomenological modeling of nanosecond pulsed plasma discharges with and without turbulence *AIAA Scitech 2022 Forum* p 0976
[29] Barléon N, Cheng L, Cuenot B and Vermorel O 2023 *Combust. Flame* **253** 112794
[30] Li C, Ebert U and Hundsdorfer W 2012 *J. Comput. Phys.* **231** 1020–50
[31] Teunissen J and Ebert U 2016 *Plasma Sources Sci. Technol.* **25** 044005
[32] Tholin F and Bourdon A 2013 *J. Phys. D: Appl. Phys.* **46** 365205
[33] Zhu Y, Shcherbanev S, Baron B and Starikovskaia S 2017 *Plasma Sources Sci. Technol.* **26** 125004
[34] Zhu Y, Chen X, Wu Y, Hao J, Ma X, Lu P and Tardiveau P 2021 *Plasma Sources Sci. Technol.* **30** 075025
[35] Johnson P N, Taneja T S and Yang S 2024 3d phenomenological modeling of plasma-assisted methane reforming *AIAA SCITECH 2024 Forum* p 0403
[36] Rusterholtz D, Lacoste D, Stancu G, Pai D and Laux C 2013 *J. Phys. D: Appl. Phys.* **46** 464010
[37] Popov N 2013 Fast gas heating initiated by pulsed nanosecond discharge in atmospheric pressure air *51st AIAA Aerospace Sciences Meeting Including the New Horizons Forum and Aerospace Exposition* p 1052
[38] Castela M, Stepanyan S, Fiorina B, Coussement A, Gicquel O, Darabiha N and Laux C O 2017 *Proc. Combust. Inst.* **36** 4095–103
[39] Bechane Y and Fiorina B 2021 *Proc. Combust. Inst.* **38** 6575–82
[40] Blanchard V P, Minesi N, Bechane Y, Fiorina B and Laux C O 2022 Experimental and numerical characterization of a lean premixed flame stabilized by nanosecond discharges *AIAA SCITECH 2022 Forum* p 2255
[41] Taneja T S, Ombrello T, Lefkowitz J and Yang S 2024 *Combust. Flame* **267** 113574
[42] Malé Q, Shcherbanev S and Noiray N 2023 *Proc. Combust. Inst.* **39** 5447–56
[43] Bechane Y and Fiorina B 2023 *Proc. Combust. Inst.* **39** 5465–76
[44] Barléon N, Cuenot B and Vermorel O 2023 *Appl. Energy Combust. Sci.* **15** 100163
[45] Malé Q, Barléon N, Shcherbanev S, Dharmaputra B and Noiray N 2024 *Combust. Flame* **260** 113206
[46] Raether H 1939 *Z. Phys.* **112** 464–89
[47] Loeb L B and Meek J M 1940 *J. Appl. Phys.* **11** 438–47
[48] Van Veldhuizen E 2000 *Electrical Discharges for Environmental Purposes: Fundamentals and Applications* (Nova Science)
[49] Starikovskiy A, Rakitin A, Correale G, Nikipelov A, Urushihara T and Shiraishi T 2012 Ignition of hydrocarbon-air mixtures with non-equilibrium plasma at elevated pressures *50th AIAA Aerospace Sciences Meeting Including the New Horizons Forum and Aerospace Exposition* p 828
[50] Yuwei F, Mengsha H, Chi C, Chuang W and Zhang Z 2023 *Plasma Sci. Technol.* **25** 085401
[51] Wang Z, Dijcks S, Guo Y, Van Der Leegte M, Sun A, Ebert U, Nijdam S and Teunissen J 2023 *Plasma Sources Sci. Technol.* **32** 085007
[52] Stephens J, Abide M, Fierro A and Neuber A 2018 *Plasma Sources Sci. Technol.* **27** 075007
[53] Pancheshnyi S 2014 *Plasma Sources Sci. Technol.* **24** 015023
[54] Marskar R 2020 *Plasma Sources Sci. Technol.* **29** 055007
[55] Lin B, Zhuang C, Cai Z, Zeng R and Bao W 2020 *Plasma Sources Sci. Technol.* **29** 125010
[56] Lo A, Cessou A, Lacour C, Lecordier B, Boubert P, Xu D, Laux C and Vervisch P 2017 *Plasma Sources Sci. Technol.* **26** 045012
[57] Wu S, Cheng W, Huang G, Wu F, Liu C, Liu X, Zhang C and Lu X 2018 *Phys. Plasmas* **25** 123507
[58] Chen X, Zhu Y and Wu Y 2020 *Plasma Sources Sci. Technol.* **29** 095006
[59] Jasak H 2009 *Int. J. Naval Archit. Ocean Eng.* **1** 89–94
[60] Millikan R C and White D R 1963 *J. Chem. Phys.* **39** 3209–13
[61] Bourdon A, Pasko V, Liu N Y, Célestin S, Ségur P and Marode E 2007 *Plasma Sources Sci. Technol.* **16** 656

[62] Luque A, Ebert U, Montijn C and Hundsdorfer W 2007 *Appl. Phys. Lett.* **90** 081501
[63] Xu D, Shneider M, Lacoste D and Laux C 2014 *J. Phys. D: Appl. Phys.* **47** 235202
[64] Poinsot T J and Lelef S 1992 *J. Comput. Phys.* **101** 104–29
[65] Lu T and Law C K 2008 *Combust. Flame* **154** 761–74
[66] Smith G P *et al* 1999 *Gas Research Institute* (available at: www.me.berkeley.edu/gri_mech)
[67] Capitelli M, Colonna G, Marraffa L, Giordano D, Giordano D and Warmbein B 2005 *tables of Internal Partition Functions and Thermodynamic Properties of High-Temperature Mars-Atmosphere Species From 50K to 50000k* (European Space Agency)
[68] Romanov G, Stankevich Y A, Stanchits L and Stepanov K 1995 *Int. J. Heat Mass Transfer* **38** 545–56
[69] Gleizes A, Razafinimanana M and Vacquie S 1986 *Plasma Chem. Plasma Process.* **6** 65–78
[70] Ritter E R 1991 *J. Chem. Inf. Comput. Sci.* **31** 400–8
[71] Jarosiński J 1983 *Combust. Flame* **50** 167–75
[72] Franklin R 2003 *J. Phys. D: Appl. Phys.* **36** R309
[73] Minesi N, Blanchard V, Pannier E, Stancu G D and Laux C O 2022 *Plasma Sources Sci. Technol.* **31** 045029
[74] Langer T, Markus D, Lienesch F and Maas U 2010 *Combust. Sci. Technol.* **182** 1718–34
[75] Bulat M, Bulat P, Denissenko P, Esakov I, Grachev L, Volkov K and Volobuev I 2018 *IEEE Trans. Plasma Sci.* **47** 57–61
[76] Shen S, Rempe E and Lefkowitz J 2023 On hydrodynamic regimes of pulse ignition in methane-air flow *AIAA Scitech 2023 Forum* p 0746
[77] Rogallo R S 1981 *Numerical Experiments in Homogeneous Turbulence* vol 81315 (National Aeronautics and Space Administration)
[78] Passot T and Pouquet A 1987 *J. Fluid Mech.* **181** 441–66